ACS NANO

www.acsnano.org

ARTICLE

Gate-Tunable Ionothermoelectric Cooling in a Solid-State Nanopore

Makusu Tsutsui,* Kazumichi Yokota, Wei-Lun Hsu,* Yuki Komoto, Denis Garoli, Hirofumi Daiguji, and Tomoji Kawai*

Cite This: *ACS Nano* 2025, 19, 41076–41085

Read Online

ACCESS | Metrics & More | Article Recommendations | Supporting Information

ABSTRACT: **Efficient heat dissipation at the nanoscale remains a major challenge for high-performance microelectronics. Here, we demonstrate a proof-of-concept approach for ionothermoelectric cooling, the ionic analogue of the Peltier effect, using gate-tunable solid-state nanopores integrated with nanoscale thermocouples. By integrating a nanoscale thermocouple directly adjacent to a gate-tunable solid-state nanopore, we quantitatively map local thermal responses driven by voltage-induced ion transport. We show that ionic heating scales with input power and varies with the ion species, revealing a dependence on the intrinsic heat of transport. Under salt concentration gradients, we observe ionic cooling, a fluidic analogue of the Peltier effect, arising from directional cation transport through negatively charged nanopores. This effect is further enhanced via electrostatic gating, which modulates the pore wall surface potential to tune the permselectivity. Under optimal gating, the system exhibits reversible transitions between heating and cooling regimes with temperature drops exceeding 2 K. Although modest compared to electronic Peltier devices, this effect establishes a viable mechanism for active, electrically tunable thermal management in nanofluidic systems. Given that water-based flow cooling already outperforms solid-state thermoelectrics by orders of magnitude, incorporating ionothermoelectric cooling can further enhance heat-pumping efficiency in micro- and nanofluidic architectures, thereby establishing a scalable on-chip ionic refrigeration strategy for next-generation semiconductor thermal control.**

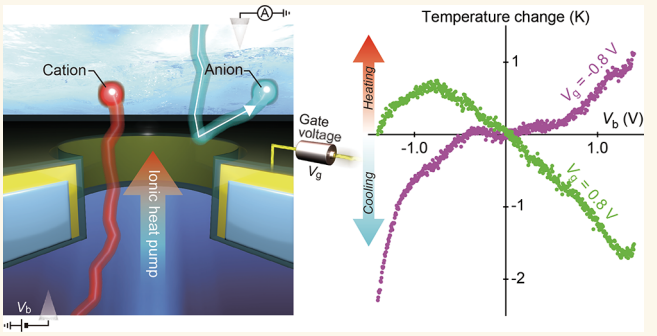

KEYWORDS: *heat dissipation, nanoscale thermocouple, Peltier effect, on-chip ionic refrigeration strategy*

INTRODUCTION

Continuous device scaling has pushed the integrated circuit technology for the sub-3 nm node,[1,2] while More-than-Moore strategies such as three-dimensional monolithic stacking have transformed chip architecture and functional density.[3] In parallel, the rise of artificial-intelligence workloads and data-centric applications has driven a surge in computation and memory traffic across hyperscale data centers.[4−6] This relentless escalation in on-chip switching activity concentrates heat in ever-smaller volumes, making energy dissipation a crucial bottleneck to further performance scaling.[7,8] For example, air-cooled heat sinks, ubiquitous in present servers, are already approaching their thermodynamic limits at power densities >100 W cm^{-2}.[9,10] Whereas state-of-the-art facilities, therefore, rely increasingly on liquid cooling, a fundamental mismatch persists between nanoscale thermal hotspots and millimeter-scale fluidic channels, leading to inefficient thermal coupling,[11] consuming vast quantities of water and thereby raising environmental concerns.[12]

Active on-chip cooling via fluid flow offers a compelling route toward thermally sustainable microelectronics. Advanced semiconductor technologies have enabled the monolithic integration of micro- and nanoscale fluidic channels beneath wafers, facilitating codesigned architectures for efficient thermal regulation.[13−16] Laminar flow within these miniaturized conduits enables precise thermal control and low interfacial resistance, outperforming conventional indirect cooling strategies.[17]

Here, we introduce an alternative and complementary approach that harnesses ionic heat transport through nanofluidic channels, drawing conceptual parallels to thermoelectric

Received: August 6, 2025
Revised: October 16, 2025
Accepted: October 16, 2025
Published: November 25, 2025

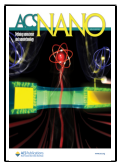

effects in solids. Analogous to the Peltier effect, where directional transport of charge carriers in a solid induces localized heating or cooling, we demonstrate that field-effect-controlled ion transport in a nanopore, which inherently carries both electrical charge and enthalpy,[18] can generate directed thermal fluxes when driven through permselective nanopores. This ionothermoelectric phenomenon enables active heat modulation in fluidic systems (Figure 1), offering potential synergy with microchannel-based convective cooling schemes for the thermal management of next-generation high-power-density processors.

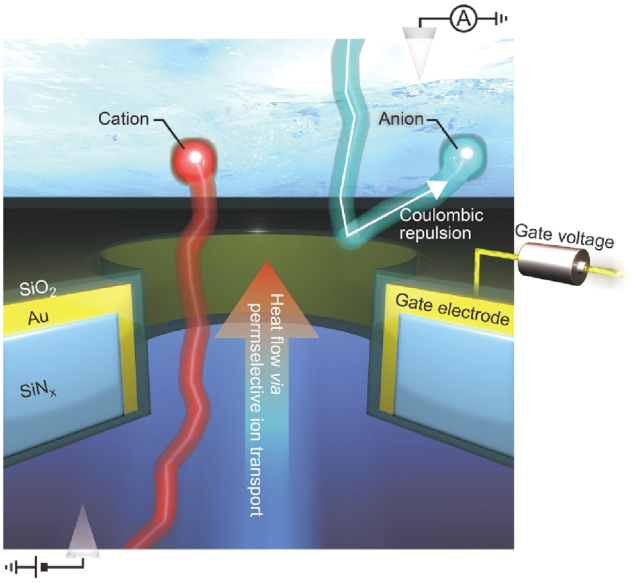

Figure 1. Schematic illustration of gate-controlled ionothermoelectric cooling in a nanopore. A gate voltage tunes the surface potential of the nanopore wall, electrostatically excluding co-ions (anions, shown in blue) and enriching counterions (cations, shown in red) near the interface (image not to scale). The resulting permselective ion flux drives directional heat transport, transferring thermal energy across the membrane and thereby realizing an ionic analogue of Peltier cooling.

RESULTS AND DISCUSSION

To probe the thermal response of field-gated ionic transport, we formed a gate-all-around nanopore[19,20] in a 70 nm thick SiN_x/SiO_2 membrane with a nanoscale Au/Pt thermocouple[21] adjacent to the Au gate electrode (Figure 2a–c, see also Figures S1–S4). The field-effect transistor-like nanofluidic architecture[22−24] allows the modulation of pore wall surface potential via the applied gate voltage V_g under given Debye screening effects,[25,26] proven effective for tuning molecular translocation,[27] ionic rectification,[28] in-pore chemical reactions,[29,30] and even permselectivity.[31,32] Meanwhile, the thermocouple generates a thermovoltage V_{th} in μV, which we calibrate to the local temperature $T_{pore} = 5.9\ V_{th} + T_0$, where T_0 = 293 K (Figure S5).[21,33] Embedding the thermocouple at the edge of a pristine nanopore has been previously shown to enable accurate local temperature measurement with errors below 5% (Figure S6). Due to the presence of the gate electrode, however, the thermal sensor needs to be positioned approximately 100 nm away from the nanopore center, slightly compromising the accuracy in estimating the in-pore temperature. Quantitatively, this design reduces the temperature sensitivity by 67% compared to a directly coupled configuration (Figures S7 and S8), a trade-off we find acceptable for resolving ion-transport-mediated local heat dissipation.

Simultaneous measurements of the ionic current I_{ion} and T_{pore} were performed under varying transmembrane voltage V_b. T_{pore} is confirmed to respond rapidly against a change in the transmembrane voltage (Figure S9) for the small volume of water with low heat capacity involved in the local ionic heat dissipation,[34] ensuring neglectable influence of thermal drift. In 1.4 M KCl, a 70 nm nanopore exhibited an ohmic $I_{ion}-V_b$ behavior, yielding a conductance G_{pore} consistent with the Maxwell−Hall model (Figure 2d).[35,36] Meanwhile, T_{pore} demonstrated a nonlinear increase with $|V_b|$, suggestive of local Joule heating via the ion electromigration under the focused electric field at the nanopore (Figure 2e,f).[37−39] Plotting against the input power $P = I_{ion}V_b$, T_{pore} is shown to rise linearly defining a constant heating rate r_h (Figure 2g). Results are found as qualitatively the same in a 1 μm micropore, except for the lower r_h indicating less efficient ionic heating in larger pores (Figure S10).

The thermal system can be modeled as a Joule heat source at the pore center connected to the thermal resistance K_i of the surrounding salt water with heat capacity c_i (Figure 2e inset). Heat flow in the thermal circuit under an input power is described as

$$\frac{T_{pore} - T_0}{P} = \frac{1}{tc + 1/K} \tag{1}$$

where K and c are the combined K_i and c_i, respectively. Since $t = 0$ at a steady state, the equation reduces to $KP = T_{pore} - T_0$, which is consistent with $r_hP = T_{pore}$ in Figure 2g. Assuming a constant thermal conductivity λ of the electrolyte solution, K is approximated by $LS^{-1}\lambda^{-1}$, with $L \sim 2d_{pore}$ and $S \sim \pi {d_{pore}}^2/4$, predicting a ~10-fold higher K for the 70 nm nanopore than the 1 μm micropore. This explains the larger Joule heating rate in the smaller pore (r_h = 8.5 and 3.9 K/μW for 70 nm and 1 μm pores, respectively), with the error ascribed in part to the difference in the relative contributions of the access resistance (Figure S10), i.e., the resistance components outside the pores, for the two pores of different aspect ratio structures.

Gating effects on ionic Joule heat dissipation are revealed to be negligible. This is shown by the $I_{ion}-$ and $T_{pore}-V_b$ characteristics remaining almost unchanged under $V_g = \pm 0.8$ V (Figure 2f, see also Figure S11). The result is consistent with the strong electrostatic screening in the high salt concentration solution that spatially confines the electric field at the pore wall to the subnanometer level.[40] The resulting little contribution of the counterion conduction on the net ionic flux gives a constant nanopore conductance and heating rate irrespective of V_g (Figure 2h).

To explore how ionic species influence the ionic Joule heat dissipation, we examined a series of mono- and multivalent electrolytes: LiCl, NaCl, KCl, RbCl, CsCl, $CaCl_2$, $MnCl_2$, and $AlCl_3$. $I_{ion}-V_b$ characteristics in 2 M solutions reveal a variation in G_{pore} reflecting the differing bulk solution conductivity of the salt solutions containing different cations of distinct mobilities (Figure 3a, see also Figures S12 and S13 for results with all types of salts).[41] Meanwhile, although one might expect heating efficiency r_h to be independent of electrolyte composition, given that salt water thermal conductivity λ is presumed to be constant, our measurements revealed a non-negligible salt dependence (Figure 3b, see also Figure S14 for

https://doi.org/10.1021/acsnano.5c13339
ACS Nano 2025, 19, 41076−41085

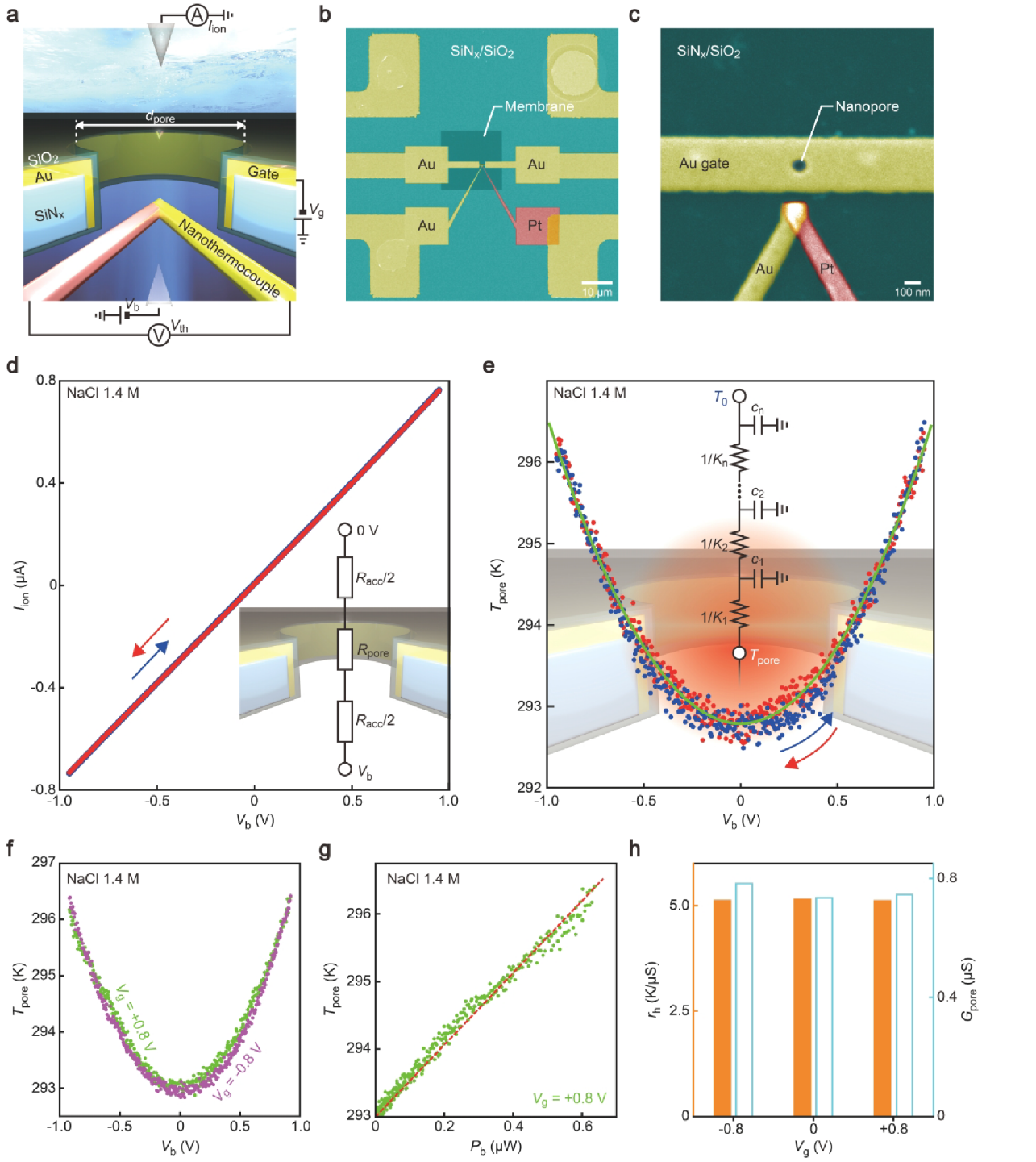

Figure 2. Negligible gating effects on in-pore ionic heat dissipation at a high slat concentration. (a) Schematic model of a thermocouple-embedded gate-all-around nanopore. Ionic current I_{ion} through the pore is measured under the applied transmembrane V_b and gate voltage V_g. (b) False-colored optical image showing a square SiN_x/SiO_2 membrane with four metal lines comprising the gate electrode and nanothermocouple. (c) False-colored scanning electron micrograph displaying the structure of the gate-all-around nanopore with the embedded thermocouple. (d) Ionic current I_{ion} through a 70 nm thermocouple-embedded gate-all-around nanopore in 1.4 M NaCl, plotted as a function of transmembrane voltage V_b. Blue and red traces indicate forward and reverse voltage sweeps, respectively. The inset shows an equivalent circuit model comprising pore resistance R_{pore} and access resistance R_{acc}. (e) Corresponding nanopore temperature T_{pore} during voltage sweeps. The green curve is a quadratic fit. (f) Nanopore heating characteristics in 1.4 M NaCl under V_g = 0.8 V (green) and −0.8 V (purple). (g) T_{pore} plotted against the input power $P = I_{ion}V_b$. The dashed line is a linear fit. (h) The nanopore heating rate r_h deduced from the slopes in the linear T_{pore} versus P characteristics. The nanopore conductance G_{pore} is also shown.

T_{pore} plotted as a function of I_{ion}). Since $r_h^{-1} \sim \lambda$ according to the thermal circuit, this suggests a change in the effective thermal conductivity by the inclusion of ions in water.[42]

The capability of ions as carriers of enthalpies in aqueous solutions is described by the heat of transport Q_{ion}.[43] Assuming no electrostatic screening by ion−ion interactions, Q_{ion} is given

https://doi.org/10.1021/acsnano.5c13339
ACS Nano 2025, 19, 41076−41085

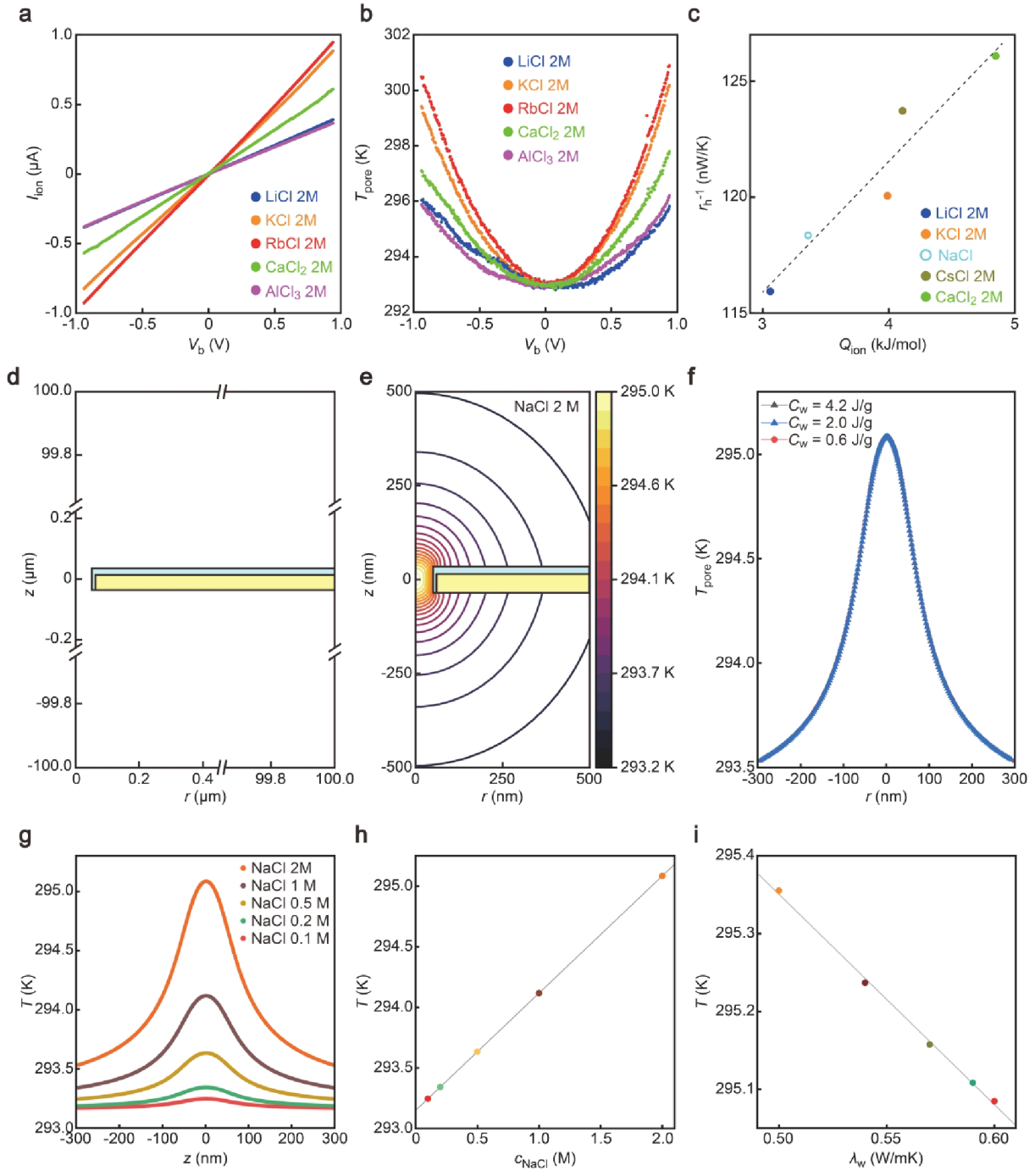

Figure 3. Ionic contribution to heat dissipation in a nanopore. (a) I_{ion}−V_b characteristics of a 70 nm thermocouple-embedded nanopore measured in 2 M solutions of different salts: LiCl (blue), KCl (orange), RbCl (red), $CaCl_2$ (green), and $AlCl_3$ (purple). (b) Corresponding nanopore temperature T_{pore} during voltage sweeps in each salt solution. Color coding follows panel a. (c) Plots of inverse heating rate r_h^{-1} against the heat of transport of ions Q_{ion}. Data are shown for the salts whose Q_{ion} values are available in the literature.[18] Dashed line is a linear fit. (d) A model used for the thermal analysis consisting of a nanopore in a SiO_2 (sky blue) /SiN_x (yellow) membrane of 70 nm thickness. (e) Temperature distribution around the nanopore by local Joule heating under transmembrane voltage of 0.9 V in 2 M NaCl. (f) Temperature distributions around the self-heated nanopore under 0.9 V in 2 M NaCl with different specific heat capacity C_w of water. The plots are superimposed with each other, manifesting the negligible influence of the solution heat capacity on the heat dissipation at steady states. (g) Temperature distributions at the self-heated nanopore under different salt concentrations at 0.9 V. (h) Nanopore temperature at z = 0 in panel d plotted as a function of the salt concentration c_{NaCl}. The gray line is a linear fit. (i) The nanopore temperature at 0.9 V in 2 M NaCl with varying liquid thermal conductivity λ_w. The gray line is a linear fit.

as $Q_{ion} = \tau q^2/8\pi\varepsilon r$, where q, ε, and r are the charge, the dielectric constant, and the radius of ions, respectively, while τ represents the temperature dependence of ε.[44] Indeed, heating rates in the equimolar solutions of different salts are found to scale with Q_{ion} as $r_h^{-1} \sim Q_{ion}$ (Figure 3c), suggesting the profound influence of ionic drift on the heat dissipation at the self-heated nanopores (only Q_{ion} available in the literature[43] is considered).

https://doi.org/10.1021/acsnano.5c13339
ACS Nano 2025, 19, 41076−41085

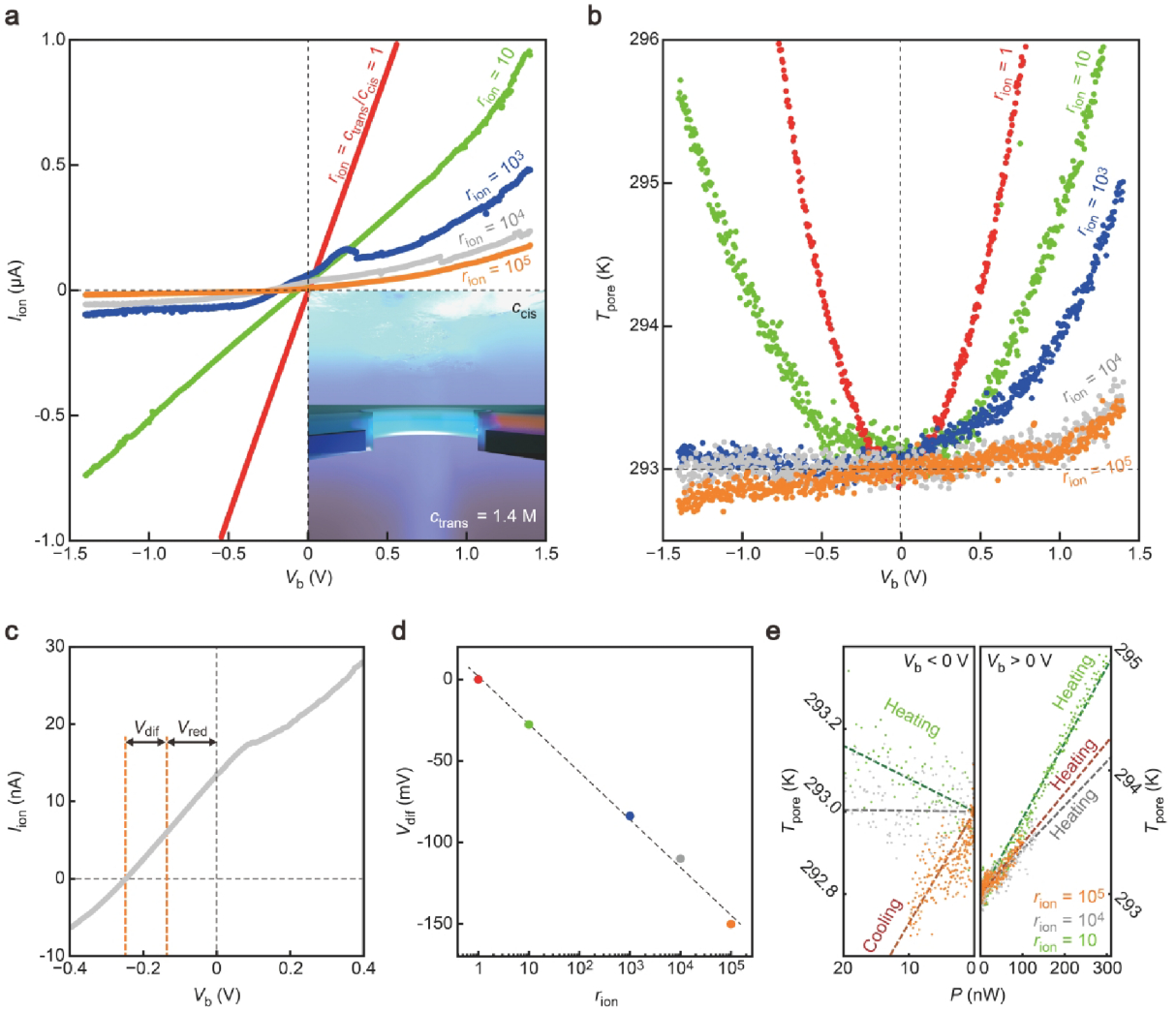

Figure 4. Ionic refrigeration in a nanopore under salinity gradients. (a) I_{ion}−V_b characteristics of a 70 nm thermocouple-embedded nanopore under transmembrane salinity gradients. The salt concentration on the cis side (c_{cis}) was varied from 1.4 M (red) to 0.00014 M (orange), while the trans side (c_{trans}) was held constant at 1.4 M. The salinity ratio $r_{ion} = c_{trans}/c_{cis}$ defines the gradient strength. (b) Corresponding changes in nanopore temperature (T_{pore}) recorded simultaneously with I_{ion}. Color coding matches panel a. (c) Close view showing the open circuit voltage derived from the redox (V_{red}) and diffusion voltage (V_{dif}) under a 10^4-fold salinity difference. (d)V_{dif}−r_{ion} dependence suggesting cation selectivity of the nanopore. (e) Plot of input power P versus T_{pore} under varying salinity gradients. Joule heating dominates at positive V_b, whereas at large r_{ion}, Peltier cooling at negative V_b leads to net refrigeration, with T_{pore} dropping below ambient at c_{cis} = 0.0014 M.

We conducted finite element simulations incorporating the coupled Poisson−Nernst−Planck, Navier−Stokes, and thermal transport equations to elucidate the origin of the observed ion-dependent heating behavior (Figure 3d, see also Figures S15 and S16).[21,39] These analyses confirmed that Joule heating, derived from diffusive ion transport via the focused electric field in the viscous media, is highly localized near the nanopore (Figure 3e). Meanwhile, while the pore conductance is estimated to increase linearly with NaCl concentration, consistent with $\sigma = ec_{NaCl}(\mu_{Na} + \mu_{Cl})$, where $\mu_{Na,Cl}$ is the mobility of Na^+ and Cl^-, the specific heat capacity of the solution is found to cause no notable change in the temperature distribution around the nanopore (Figure 3f). Moreover, when the thermal conductivity λ_w of the electrolyte was held constant, the simulated heating rate remained unchanged across a range of c_{NaCl} values examined (Figure 3g,h). Changing λ_w from 0.56 W/mK, on the other hand, alters the local heating efficiency as $r_h^{-1} \sim \lambda_w$ (Figure 3i, see also Figure S17). These results support the accuracy of the thermal circuit model in Figure 2e, corroborating the notable roles of ion transport in the experimentally observed variations in r_h.

Direct evidence of ion-mediated heat transport emerged under salt gradients across permselective nanopores (Figure 4a,b). Diluting the salt water expands the electrostatic potential distributions by the surface charges on the membrane surface to render charge-selective ion transport in the pore.[45,46] This is seen as an increase in the open circuit voltage V_{off} in the I_{ion}−V_b curves upon decreasing the ion concentration c_{cis} at the cis side (Figure 4a). More quantitatively, V_{off} under the salinity gradients is given as $V_{off} = V_{red} + V_{dif}$ (Figure 4c), where V_{red} and V_{dif} are the redox voltage at the electrode and the transmembrane electric potential difference generated by the diffusive ion transport, respectively (V_{red} is estimated as shown in Figures S18 and S19).[47] Here, V_{dif} is nearly zero in a nonpermselective nanopore, as diffusion of the equivalent amounts of anions and cations induces negligible voltage.[45] On

https://doi.org/10.1021/acsnano.5c13339
ACS Nano 2025, 19, 41076−41085

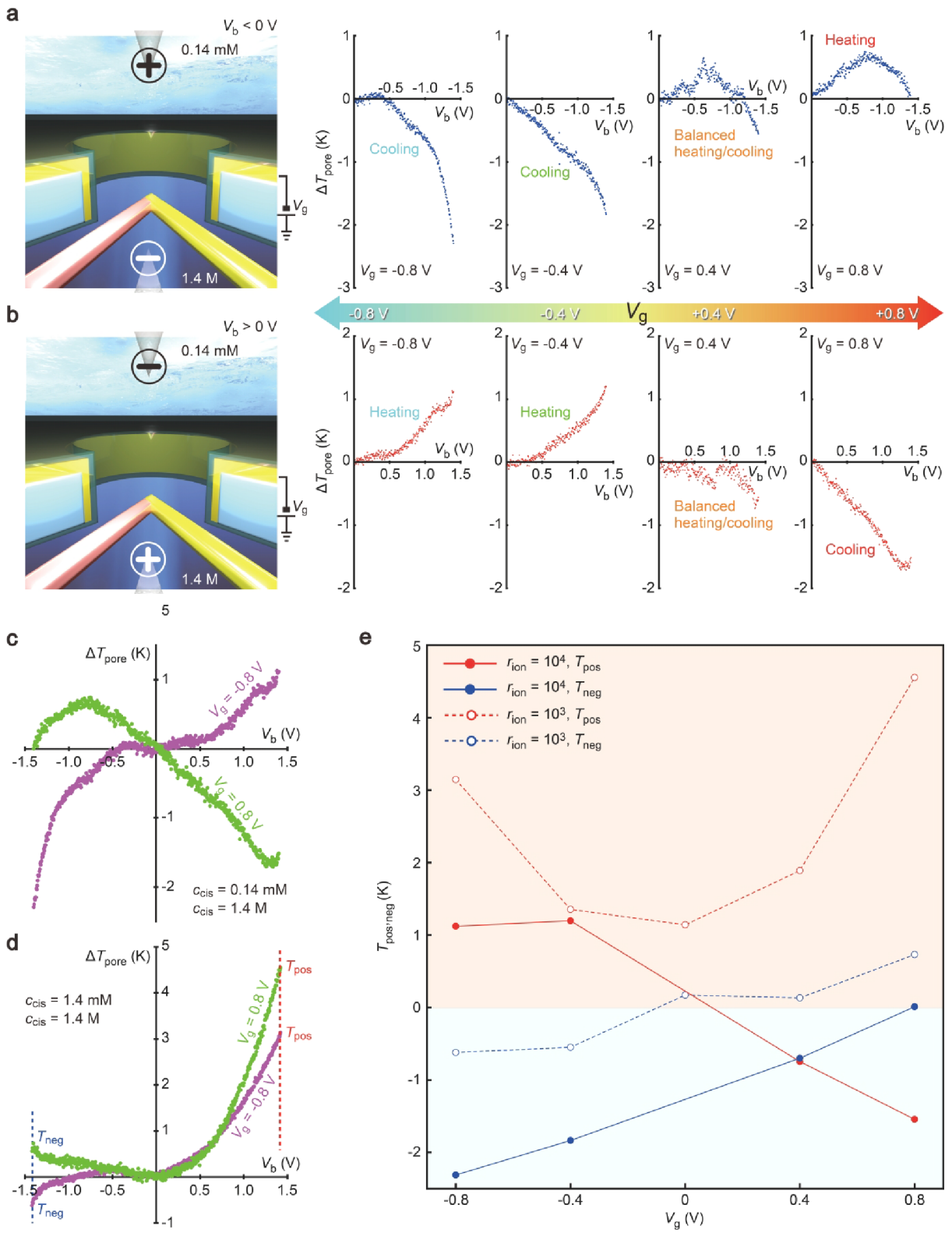

Figure 5. Field-effect modulation of ionic heat dissipation in a nanopore. (a, b) Temperature variations ΔT_{pore} with respect to room temperature in response to V_g modulation in a 70 nm nanopore under positive (a) and negative (b) transmembrane voltage. The gate bias dynamically alters the ionic heating profile depending on the direction of ion transport. (c, d) ΔT_{pore}–V_b characteristics at r_{ion} = 10^4 (c) and 10^3 (d) under V_g = +0.8 V (green) and −0.8 V (purple). $T_{pos,neg}$ denotes the temperature at V_b = 1.4 and −1.4 V, respectively. (e) Plots of $T_{pos,neg}$ as a function of V_g. Blue and red regions denote nanopore cooling and heating via the V_g-derived permselective ion transport.

the contrary, selective ion transport through the pore provides finite diffusion potential reflecting the permselectivity as denoted by the Nernst equation, $V_{dif} = S_{ion}(k_BT/e)\ \ln(a_{cis}/a_{trans})$, where S_{ion} is the coefficient defining the magnitude of permselectivity with S_{ion} = +1 and −1 for the case of perfect cation and anion selectivity and 0 for nonselective transport.[48]

https://doi.org/10.1021/acsnano.5c13339
ACS Nano 2025, 19, 41076−41085

Assuming the ion activity at the cis and trans, $a_{cis,trans}$,[49] to be approximated as c_{cis} and c_{trans}, V_{dif} is obtained by subtracting V_{red}, which decreased to below 0 V with decreasing c_{cis} (Figure 4d). It indicates the cation-selective transport in the nanopore, consistent with the negative native charges on the SiO_2 membrane surface causing Coulombic repulsion of anions at the orifice to hinder their translocation.

The permselectivity induces ionic current rectification. Under positive transmembrane voltage, high concentration Na^+ flows from the trans to cis side, resulting in a high G_{pore}. In contrast, at negative voltage, the Cl^- flux is impeded by electrostatic repulsion from the negatively charged membrane surface. Consequently, the nanopore admits only dilute Na^+ flux, thereby suppressing I_{ion}.[50] No matter the rectifying behavior, the Joule heat becomes smaller as the ionic conductance is lowered with decreasing c_{cis}, giving rise to weaker changes in T_{pore} under the V_b scans (Figure 4b). Notably, meanwhile, it exhibits refrigeration at r_{ion} larger than 10^4, where T_{pore} falls below ambient temperature under negative V_b,[51] highlighting the predominant role of ionic heat of transport (Figure 4e). This active cooling is attributed to enhanced cation selectivity at low c_{cis}, which promotes the Na^+-selective transport-mediated unidirectional heat flow, i.e., an ionic analogue of the Peltier effect, to outweigh its contribution over the counteracting Joule heating.

Because permselectivity is essential for enabling ion-driven thermoelectric effects, a refrigeration behavior is absent in larger pores where selectivity is minimal. For instance, in a 1 μm-diameter micropore, imposing a salt concentration gradient results in pronounced ionic current rectification, including signatures of negative differential resistance (Figure S20), arising from electroosmotic flow-induced modulation of local ion concentrations.[52] Although the current−voltage characteristics superficially resemble those observed in nanopores, no signs of ionic cooling are detected, attributed to the negligible permselectivity in the micrometer-scale conduit, where the electric double layer is too thin relative to the pore size to exert significant electrostatic control over ion transport (Figures S20 and S21).

The gating effect offers a powerful means for the active control of ionothermoelectric transport, particularly under low ionic strength conditions where counterion transport is highly sensitive to surface potential modulation by the gate voltage.[31] With a 10^4-fold salinity gradient, the intrinsic negative surface charge of the nanopore in the absence of gating renders it cation-selective, leading to weak cooling at negative transmembrane bias via Na^+-dominated transport. Applying a negative gate voltage enhances this cation selectivity, as demonstrated by the V_{off} shifting to more negative values (Figure S22), modestly increasing the cooling efficiency as V_g is tuned from −0.4 to −0.8 V (Figure 5a). In contrast, a positive V_g inverts the wall potential, modulating the permselectivity. At V_g = +0.4 V, the opposing effects of ionothermoelectric cooling and Joule heating approximately cancel, resulting in a negligible net temperature change. Increasing the V_g to +0.8 V further modulates the surface potential toward anion selectivity and ultimately reverses the thermal response from heating to cooling. Meanwhile, the local temperature exhibits distinct responses to positive and negative V_g reflecting the differing contributions of sodium and chloride counterions due to their intrinsic differences in heat of transport (3.5 versus 0.5 kJ/mol) and diffusivity (1.3×10^{-9} versus 2.0×10^{-9} m^2/s).

Because the majority carrier switches polarity with the direction of V_b, the gating effect is reversed under positive bias (Figure 5b): ionic heating is amplified by negative V_g, while positive V_g enhances cooling. This gate-controlled thermoelectric response is more pronounced in dilute electrolytes. At a salinity ratio of $r_{ion} = 10^4$, applying ±0.8 V to the gate electrode effectively switches the thermal response from heating to cooling (Figure 5c). In contrast, under a reduced salinity gradient ($r_{ion} = 10^3$), the gating effect is attenuated: while negative V_g still induces notable cooling at negative bias, it has minimal impact on Joule heating at positive V_b (Figure 5d, see also Figure S23).

To highlight these effects, we plotted the nanopore temperature at V_b = +1.4 V (T_{pos}) and −1.4 V (T_{neg}) as a function of the gate voltage (Figure 5e). Sign changes in T_{pos} and T_{neg} mark the transition between heating and cooling driven by permselectivity inversion. Noticeably, at $r_{ion} = 10^4$ and V_g = −0.8 V, T_{neg} exceeds −2 K (Figure S24), nearly 3 times greater than the corresponding value at $r_{ion} = 10^3$ (we note that this T_{neg} underestimates the actual temperature inside the nanopore by approximately 70%, anticipating local refrigeration by more than 3 K). These results establish that ion-driven heat transport can be actively and reversibly modulated via electrostatic gating, providing a programmable platform for nanoscale thermal control.

CONCLUSIONS

This study demonstrates that ionic heat transport in nanopores is not merely a passive consequence of Joule heating but a controllable phenomenon with functional relevance for nanoscale thermal management. Under an applied bias, each ion drags a certain amount of heat along with its charge. Thus, directional ion flow can carry away the enthalpy from the nanopore region. In a nonselective pore, cations and anions migrate in opposite directions, and their transported heats cancel out, yielding no net cooling. By contrast, a permselective pore passes almost only one type of ion so that ionic enthalpy is carried predominantly in one direction, pumping heat out of the nanopore and lowering its local temperature. This mechanism is the ionic analogue of the Peltier effect, where the voltage-driven counterion flux extracts enthalpy from the pore and releases that heat on the far side, producing a localized cooling effect. The gate electrode in this study actively tunes the permselectivity by modulating the surface charge. As a result, the thermal response is reversible and gate-controllable. This cooling is highly localized to the nanoscale vicinity of the pore since the region of enthalpy removal is confined to the tiny nanopore and immediate fluid around it. However, energy is fully conserved since the extracted heat is expelled into the surrounding environment or downstream fluid by the ion flow. In other words, the electrical work performed on the ions drives a heat current from the nanopore to the external reservoirs. So while the nanopore cools, an equivalent amount of heat is dissipated to warm the bulk solution. Importantly, any Joule heating from the ionic current occurs in parallel and tends to heat the pore. As such, net cooling is observed only when the enthalpy carried away by the selective ion flux outweighs local Joule heating.

Previous studies have shown voltage-controlled ionic rectification using confined nanopore systems. For instance, nanopore electrode arrays via a cation-exchange overlayer and top electrode achieved a voltage-switched diode behavior by electrochemical gating.[53] Attoliter-scale encapsulated nano-

https://doi.org/10.1021/acsnano.5c13339
ACS Nano 2025, 19, 41076−41085

pores demonstrated rectification arising from ion migration under strong confinement.[54] In contrast, the present gate-tunable solid-state nanopore integrates direct electrostatic gating within a single-pore platform, unifying active charge modulation with nanoscale confinement. This architecture allows the dynamic inversion of ionic permselectivity and extends the rectification concept to controllable ionothermoelectric cooling, a functionality beyond purely electrical gating.

Permselectivity and ionic conductance in a nanopore are found to be important factors affecting the efficiency of ionothermoelectric cooling. Without ion selectivity, anions and cations pass through a conduit under the applied voltage. As heat is carried in opposite directions by the migrating ions, it causes a negligible temperature difference across the membrane. On the contrary, the unidirectional flux of anions or cations in a permselective pore pumps heat via the voltage-driven ion transport to induce ionic cooling. In this work, refrigeration occurred under a large salinity difference, leveraging the depressed ion concentration around the pore that augmented the Coulombic co-ion repulsion from the charged wall surface to render stronger ion selectivity. The fact that r_{ion} of 10^4 allowed a more pronounced decrease in T_{pore} than with $r_{ion} = 10^3$ manifests this mechanism, where the former condition rendered stronger permselectivity to enable more efficient heat pumping by the selective ion transport. Meanwhile, although excessive dilution of salt solutions serves to further enhance the selectivity, it also entails ion depression, thereby weakening the ionic cooling effect (Figure S25). Besides these contributions, ionic Joule heating counteracts the ionic Peltier effect, complicating the energy dissipation phenomenon in nanopores.

These findings bridge the gap between thermal and ionic transport in nanoscale systems, highlighting the potential for ionothermoelectrics, a field that may complement electronic thermoelectricity in soft, aqueous, or biological environments. As the mechanism stems primarily from the selective ion transport, it can, in principle, be implemented not only in silicon nitrides but also in a wide range of membrane materials provided that their surface charge density is sufficiently high to impart strong permselectivity to nanopores. While demonstrating large-area cooling using multinanopore membranes remains an essential step toward practical implementation, the full compatibility of solid-state nanopores with semiconductor fabrication technologies promises the ion-mediated heat modulation to be harnessed for enhancing cooling efficiency in micro/nanochannel systems integrated for the on-chip thermal management.

METHODS

Fabrication of Thermocouple-Embedded Nanopores. A 4 in. Si wafer with 50 nm thick SiN_x layers coated on the surfaces was diced into 25 × 25 mm chips with a dicer. Microelectrodes were patterned on the chips by photolithography with the AZ5206-E photoresist followed by metal deposition by radio frequency magnetron sputtering. As a result, Au microelectrodes were formed by sonication in *N*,*N*-dimethylformamide (DMF) for lift-off. A nanowire was delineated by electron beam lithography with the ZEP520A electron beam resist, whose one end was overlapped with one of the microelectrodes. Subsequently, Pt was deposited by the sputtering and lifted off in DMF. The same process was carried out to create the Au nanowire, whose position was aligned with respect to a lithography-defined marker to form a point contact with the Pt nanowire. After the nanowire thermocouple was formed, a circle was patterned at the vicinity of the point contact by the electron beam lithography with ZEP520A. After development, the residual resist layer was used as a mask to drill a pore in the SiN_x membrane by reactive ion etching. Finally, the top surface was coated with 20 nm thick SiO_2 by chemical vapor deposition.

Fabrication of Thermocouple-Embedded Gate-All-Around Nanopores. Most of the fabrication processes are the same as those for fabricating thermocouple-embedded nanopores. One difference lies in the second EB lithography to form a Au nanowire. To form a gate electrode, a rectangular pattern was drawn along with the nanowire. By this, a Au gate electrode and a nanowire were created simultaneously by depositing Au and lift-off in DMF. Furthermore, to drill a pore through the Au/SiN_x layer by EB lithography and reactive ion etching, the etching time was adjusted to be longer than that for creating SiN_x nanopores.

Flow Cell Integration. The nanopore chips were sealed with flow cells made of polydimethylsiloxane (PDMS). The cells were composed of 15 × 15 × 10 mm blocks with a microfluidic channel patterned on one side of the surfaces. To form the cells, a mold was fabricated by creating I-shaped patterns on a Si wafer by photolithography with an SU-8 photoresist. Sylgard 184 was poured on the mold placed on a Petri dish and cured in an oven at 90 °C for 9 h. The blocks were cut out with a surgical knife. In each block, three holes were punched to inject salt solutions as well as to place a Ag/AgCl rod for ionic current measurements. For sealing, the PDMS block and the nanopore chip were exposed to oxygen plasma for surface activation. Subsequently, they were put together for bonding. This process was repeated once again to seal the chip from both sides.

Simultaneous Measurement of Ionic Current and Nanopore Temperature Measurements under Gate Voltage. The nanopore chip was mounted on a sample holder. Metal pins were contacted by the microelectrode pads on the chip. Two of the pins connected to the Au/Pt nanowire thermocouple were wired to a Keithley 2182A nanovoltmeter (Keithley) for the nanopore temperature measurements, while one connected to the gate electrode was wired to a picoammeter-source unit Keithley 6487 (Keithley) for the application of the gate voltage. Meanwhile, salt solutions were poured into the pore by injecting through one of the three holes in each of the two PDMS cells using a pipet. After that, Ag/AgCl rods were placed at both sides. Transmembrane voltage was applied to one of the rods, and the resulting ionic current was measured through the other rod using another Keithley 6487. The thermovoltage and ionic current were recorded simultaneously under the transmembrane voltage ramps, and the gate voltage was controlled through GPIB with a program coded in Visual Basic.

Thermocouple Calibration. The thermovoltage V_{th} at the thermocouple was measured under substrate heating with an electrical heater to a constant temperature using a temperature controller. The relationship between V_{th} (in μV) and the substrate temperature T_s gives an equation $T_s = 5.9V_{th} + T_0$ for converting the thermovoltage to the local temperature at the point contact, where $T_0 = 293$ K is the ambient temperature.

Redox Potential Measurement. $I_{ion}-V_b$ characteristic measurements were performed on a 3 μm micropore in a 50 nm thick SiN_x membrane with the cis and trans compartments filled with NaCl solutions of salt concentrations c_{cis} and c_{trans}. Specifically, c_{trans} was kept at 1.4 M while changing c_{cis} from 1.4 to 0.000014 M. The redox potential was obtained from the open circuit voltage at the zero current intersections in the $I_{ion}-V_b$ curves.

Finite Element Analysis. To model the temperature distribution within a nanopore under applied cross-membrane voltage, we employed finite element simulations based on heat transfer equations incorporating Joule heating.[21] The steady-state heat equation was defined separately for (eq 2) solids and (eq 3) fluids as follows:

$$\nabla\cdot(\kappa\nabla T) + J\cdot E = 0 \tag{2}$$

$$\nabla\cdot(\kappa\nabla T) + J\cdot E = \rho_d C_p u\cdot\nabla T \tag{3}$$

where J and E are the current density and electric field, respectively. Here, κ is the thermal conductivity, T is the temperature, ρ_d is the fluid density, C_p is the specific heat capacity, and u is the velocity field

https://doi.org/10.1021/acsnano.5c13339
ACS Nano 2025, 19, 41076−41085

of the fluid. The current density J was determined from the steady-state continuity equation. Assuming Ohm's law, the current density was linked to the electric field by $J = \sigma E$, with σ being the electrical conductivity given by $\sigma = (\mu_a c_a + \mu_c c_c)F$, where $\mu_a = 7.9 \times 10^{-8}$ m^2 V^{-1} s^{-1} and $\mu_c = 5.194$ m^2 V^{-1} s^{-1} are the mobilities of Cl^- and Na^+, respectively, while F is the Faraday constant. The steady-state spatial distributions of anions and cations (n_a, n_c) were computed by using the Nernst–Planck equation. The electric field E was solved using the nonlinear Poisson–Boltzmann equation considering the temperature-dependent permittivity of water as $\varepsilon_w = (249 - 0.790T + 7.30 \times 10^{-4}T^2)\varepsilon_0$, with ε_0 being the vacuum permittivity. Electroosmotic flow was modeled by solving the incompressible Navier–Stokes equation. All equations were simultaneously solved using the COMSOL Multiphysics 6.3 software package (COMSOL Inc., Stockholm, Sweden).

ASSOCIATED CONTENT

Data Availability Statement

The data sets generated and/or analyzed during the current study are available from the corresponding authors on reasonable request.

Supporting Information

The Supporting Information is available free of charge at https://pubs.acs.org/doi/10.1021/acsnano.5c13339.

Fabrication flowchart and SEM images of thermocouple-embedded nanopores with and without gate electrodes; evaluation of errors in the local temperature assessments; measurements of leakage current through gate electrodes; finite element analyses of temperature distributions around Joule heated nanopores; and reproducibility of field-effect-controlled ionothermoelectric cooling (PDF)

AUTHOR INFORMATION

Corresponding Authors

Makusu Tsutsui − *SANKEN, The University of Osaka, Osaka, Ibaraki 567-0047, Japan;* orcid.org/0000-0002-4552-1163; Email: makusu32@sanken.osaka-u.ac.jp

Wei-Lun Hsu − *Department of Mechanical Engineering, The University of Tokyo, Tokyo 113-8656, Japan;* orcid.org/0000-0002-5451-4301; Email: wlhsu@thml.t.u-tokyo.ac.jp

Tomoji Kawai − *SANKEN, The University of Osaka, Osaka, Ibaraki 567-0047, Japan*; Email: kawai@sanken.osaka-u.ac.jp

Authors

Kazumichi Yokota − *National Institute of Advanced Industrial Science and Technology, Takamatsu, Kagawa 761-0395, Japan;* orcid.org/0000-0002-8590-2737

Yuki Komoto − *SANKEN, The University of Osaka, Osaka, Ibaraki 567-0047, Japan;* orcid.org/0000-0002-9004-3797

Denis Garoli − *Optoelectronics Research Line, Istituto Italiano di Tecnologia, Genova I-16163, Italy; Dip. di Scienze e Metodi dell'Ingegneria, Università di Modena e Reggio Emilia via Amendola 2, Reggio, Emilia 42122, Italy;* orcid.org/0000-0002-5418-7494

Hirofumi Daiguji − *Department of Mechanical Engineering, The University of Tokyo, Tokyo 113-8656, Japan;* orcid.org/0000-0001-6896-3282

Complete contact information is available at: https://pubs.acs.org/10.1021/acsnano.5c13339

Author Contributions

All authors discussed the data and reviewed the manuscript.

Notes

The authors declare no competing financial interest.

ACKNOWLEDGMENTS

A part of this work was supported by the Japan Society for the Promotion of Science (JSPS) KAKENHI grants 23K22681, 24K21715, and 25K01639. M.T. acknowledges support from the Kansai Research Foundation for Technology Promotion.

REFERENCES

(1) Moore, S. K. The Node is Nonsense. *IEEE Spectrum* **2020**, *57*, 24–30.

(2) Zeng, S.; Liu, C.; Zhou, P. Transistor Engineering Based on 2D Materials in the Post-Silicon Era. *Nat. Rev. Elect. Eng.* **2024**, *1*, 335–348.

(3) Zhang, Y.; Udrea, F.; Wang, H. Multidimensional Device Architectures for Efficient Power Electronics. *Nat. Electron.* **2022**, *5*, 723–734.

(4) Masanet, E.; Shehabi, A.; Lei, N.; Smith, S.; Koomey, J. Recalibrating Global Data Center Energy-Use Estimates. *Science* **2020**, *367*, 984–986.

(5) Guo, C.; Luo, F.; Cai, Z.; Dong, Z. Y. Integrated Energy Systems of Data Centers and Smart Grids: State-of-the-Art and Future Opportunities. *Appl. Ene.* **2021**, *301*, No. 117474.

(6) Kaack, L. H.; Donti, P. L.; Strubell, E.; Kamiya, G.; Creutzig, F.; Rolnick, D. Aligning Artificial Intelligence with Climate Change Mitigation. *Nat. Clim. Chan.* **2022**, *12*, 518–527.

(7) Kong, R.; Zhang, H.; Tang, M.; Zou, H.; Tian, C.; Ding, T. Enhancing Data Center Cooling Efficiency and Ability: A Comprehensive Review of Direct Liquid Cooling Technologies. *Energy* **2024**, *308*, No. 132846.

(8) Yuan, X.; Zhou, X.; Pan, Y.; Kosonen, R.; Cai, H.; Gao, Y.; Wang, Y. Phase Change Cooling in Data Centers: A Review. *Ene. Bldg.* **2021**, *236*, No. 110764.

(9) Habibi Khalaj, A.; Halgamuge, S. K. A Review on Efficient Thermal Management of Air- and Liquid-Cooled Data Centers: From Chip to the Cooling System. *Appl. Ene.* **2017**, *205*, 1165–1188.

(10) Arumuru, V.; Rajput, K.; Nandan, R.; Rath, P.; Das, M. A Novel Synthetic Jet Based Heat Sink with PCM Filled Cylindrical Fins for Efficient Electronic Cooling. *J. Ene. Stor.* **2023**, *58*, No. 106376.

(11) Yu, Z. Q.; Li, M. T.; Cao, B. Y. A Comprehensive Review on Microchannel Heat Sinks for Electronics Cooling. *Int. J. Ext. Manufact.* **2024**, *6*, No. 022005.

(12) Siddik, M. A. B.; Shehabi, A.; Marston, L. The Environmental Footprint of Data Centers in the United States. *Environ. Res. Lett.* **2021**, *16*, No. 064017.

(13) van Erp, R.; Soleimanzadeh, R.; Nela, L.; Kampitsis, G.; Matioli, E. Co-Designing Electronics with Microfluidics for More Sustainable Cooling. *Nature* **2020**, *585*, 211–216.

(14) Rangarajan, S.; Schiffres, S. N.; Sammakia, B. A Review of Recent Developments in "On-Chip" Embedded Cooling Technologies for Heterogeneous Integrated Applications. *Engineering* **2023**, *26*, 185–197.

(15) Shi, H.; Grall, S.; Yanagisawa, R.; Jalabert, L.; Paul, S.; Kim, S. H.; Viovy, J. L.; Daiguji, H.; Nomura, M. Chip Cooling with Manifold-Capillary Structures Enables 10^5 COP in Two-Phase Systems. *Cell Rep. Phys. Sci.* **2025**, *6*, No. 102520.

(16) Wu, K.; Dou, Z.; Deng, S.; Wu, D.; Zhang, B.; Yang, H.; Li, R.; Lei, C.; Zhang, Y.; Fu, Q.; Yu, G. Mechanochemistry-Mediated Colloidal Liquid Metals for Electronic Device Cooling at Kilowatt Levels. *Nat. Nanotechnol.* **2025**, *20*, 104–111.

(17) Kong, R.; Zhang, H.; Tang, M.; Zou, H.; Tian, C.; Ding, T. Enhancing Data Center Cooling Efficiency and Ability: A Comprehensive Review of Direct Liquid Cooling Technologies. *Energy* **2024**, *308*, No. 132846.

(18) Helfand, E.; Kirkwood, J. G. Theory of the Heat of Transport of Electrolytic Solutions. *J. Chem. Phys.* **1960**, *32*, 857−866.
(19) Nam, S.-W.; Rooks, M. J.; Kim, K.-B.; Rossnagel, S. M. Ionic Field Effect Transistors with Sub-10 nm Multiple Nanopores. *Nano Lett.* **2009**, *9*, 2044−2048.
(20) Ren, R.; Zhang, Y.; Nadappuram, B. P.; Akpinar, B.; Klenerman, D.; Ivanov, A. P.; Edel, J. B.; Korchev, Y. Nanopore Extended Field-Effect Transistor for Selective Single-Molecule Biosensing. *Nat. Commun.* **2017**, *8*, 586.
(21) Tsutsui, M.; Arima, A.; Yokota, K.; Baba, Y.; Kawai, T. Ionic Heat Dissipation in Solid-State Pores. *Sci. Adv.* **2022**, *8*, No. abl7002.
(22) Daiguji, H.; Oka, Y.; Shirono, K. Nanofluidic Diode and Bipolar Transistor. *Nano Lett.* **2005**, *11*, 2274−2280.
(23) Paik, K.-H.; Liu, Y.; Tabard-Cossa, V.; Waugh, M. J.; Huber, D. E.; Provine, J.; Howe, R. T.; Dutton, R. W.; Davis, R. W. Control of DNA Capture by Nanofluidic Transistors. *ACS Nano* **2012**, *6*, 6767−6775.
(24) Wang, Y.; Zhang, H.; Kang, Y.; Zhu, Y.; Simon, G. P.; Wang, H. Voltage-Gated Ion Transport in Two-Dimensional Sub-1 nm Nanofluidic Channels. *ACS Nano* **2019**, *13*, 11793−11799.
(25) Daiguji, H. Ion Transport in Nanofluidic Channels. *Chem. Soc. Rev.* **2010**, *39*, 901−911.
(26) Siwy, Z. S.; Howorka, S. Engineered Voltage-Responsive Nanopores. *Chem. Soc. Rev.* **2010**, *39*, 1115−1132.
(27) Ren, R.; Wang, X.; Cai, S.; Zhang, Y.; Korchev, Y.; Ivanov, A. P.; Edel, J. B. Selective Sensing of Proteins Using Aptamer Functionalized Nanopore Extended Field-Effect Transistors. *Small Methods* **2020**, *4*, 2000356.
(28) Guan, W.; Fan, R.; Reed, M. A. Field-Effect Reconfigurable Nanofluidic Ionic Diodes. *Nat. Commun.* **2011**, *2*, 506.
(29) Fu, K.; Kwon, S.-R.; Han, D.; Bohn, P. W. Single Entity Electrochemistry in Nanopore Electrode Arrays: Ion Transport Meets Electron Transfer in Confined Geometries. *Acc. Chem. Res.* **2020**, *53*, 719−728.
(30) Reitemeier, J.; Metro, J.; Fu, K. X. Nanopore Sensing and Beyond: Electrochemical Systems for Optically-Coupled Single-Entity Studied, Stimulus-Responsive Gating Applications, and Point-of-Care Sensors. *Sens. Act. Rep.* **2024**, *8*, No. 100225.
(31) Tsutsui, M.; Hsu, W.-L.; Garoli, D.; Leong, I. W.; Yokota, K.; Daiguji, H.; Kawai, T. Gate-All-Around Nanopore Osmotic Power Generators. *ACS Nano* **2024**, *18*, 15046−15054.
(32) Lei, X.; Zhang, J.; Hong, H.; Liu, Z.; Huang, Y.; Xia, F.; Mao, L.; Jiang, L. Ultrahigh-Performance Osmotic Power Generation in Gate-Controlled Nanopores. *Adv. Funct. Mater.* **2025**, *35*, 2500989.
(33) Majumdar, A.; Lai, J.; Chandrachood, M.; Nakabeppu, O.; Wu, Y.; Shi, Z. Thermal Imaging by Atomic Force Microscopy Using Thermocouple Cantilever probes. *Rev. Sci. Instrum.* **1995**, *66*, 3584−3592.
(34) Tsutsui, M.; Hsu, W.-L.; Yokota, K.; Komoto, Y.; Daiguji, H.; Kawai, T. On-Site Unzipping of Single-Molecule DNA in a Spot-Heated Nanopore. *ACS Nano* **2025**, *19*, 28900−28912.
(35) Garaj, S.; Hubbard, W.; Reina, A.; Kong, J.; Branton, D.; Golovchenko, J. A. Graphene as a Subnanometre Trans-Electrode Membrane. *Nature* **2010**, *467*, 190−193.
(36) Sahu, S.; Zwolak, M. Maxwell-Hall Access Resistance in Graphene Nanopores. *Phys. Chem. Chem. Phys.* **2018**, *20*, 4646−4651.
(37) Chen, D. P.; Eisenberg, R. S.; Jerome, J. W.; Shu, C. W. Hydrodynamic Model of Temperature Change in Open Ionic Channels. *Biophys. J.* **1995**, *69*, 2304−2322.
(38) Nagashima, G.; Levine, E. V.; Hoogerheide, D. P.; Burns, M. M.; Golovchenko, J. A. Superheating and Homogeneous Single Bubble Nucleation in a Solid-State Nanopore. *Phys. Rev. Lett.* **2014**, *113*, No. 024506.
(39) Paul, S.; Hsu, W.-L.; Ito, Y.; Daiguji, H. Boiling in Nanopores Through Localized Joule Heating: Transition Between Nucleate and Film Boiling. *Phys. Rev. Res.* **2022**, *4*, No. 043110.
(40) Lee, C.; Joly, L.; Siria, A.; Biance, A.-L.; Fulcrand, R.; Bocquet, L. Large Apparent Electric Size of Solid-State Nanopores due to Spatially Extended Surface Conduction. *Nano Lett.* **2012**, *12*, 4037−4044.
(41) Koneshan, S.; Rasaiah, J. C.; Lynden-Bell, R. M.; Lee, S. H. Solvent Structure, Dynamics, and Ion Mobility in Aqueous Solutions at 25 °C. *J. Phys. Chem. B* **1998**, *102*, 4193−4204.
(42) Scott, J. F.; Bohn, H. G.; Schenk, W. Ionic Wiedemann-Franz Law. *Appl. Phys. Lett.* **2000**, *77*, 2599−2600.
(43) Agar, J. N.; Mou, C. Y.; Lin, J.-L. Single-Ion Heat of Transport in Electrolyte Solutions. *A Hydrodynamic Theory. J. Phys. Chem.* **1989**, *93*, 2079−2082.
(44) Zhao, D.; Würger, A.; Crispin, X. Ionic Thermoelectric Materials and Devices. *J. Ene. Chem.* **2021**, *61*, 88−103.
(45) Rollings, R. C.; Kuan, A. T.; Golovchenko, J. A. Ion Selectivity of Graphene Nanopores. *Nat. Commun.* **2016**, *7*, 11408.
(46) Tsutsui, M.; Yokota, K.; Leong, I. W.; He, Y.; Kawai, T. Sparse Multi-Nanopore Osmotic Power Generators. *Cell Rep. Phys. Sci.* **2022**, *3*, No. 101065.
(47) Kim, D.-K.; Duan, C.; Chen, Y.-F.; Majumdar, A. Power Generation From Concentration Gradient by Reverse Electrodialysis in Ion-Selective Nanochannels. *Microfluid. Nanofluid.* **2010**, *9*, 1215−1224.
(48) Zhang, S.; Wang, J.; Yaroshchuk, A.; Du, Q.; Xin, P.; Bruening, M. L.; Xia, F. Addressing Challenges in Ion-Selectivity Characterization in Nanopores. *J. Am. Chem. Soc.* **2024**, *146*, 11036−11042.
(49) Feng, J.; Graf, M.; Liu, K.; Ovchinnikov, D.; Dumcenco, D.; Heiranian, M.; Nandigana, V.; Aluru, N. R.; Kis, A.; Radenovic, A. Single-Layer MoS_2 Nanopores as Nanopower Generators. *Nature* **2016**, *536*, 197−200.
(50) Lin, C. Y.; Turker Acar, E.; Polster, J. W.; Lin, K.; Hsu, J. P.; Siwy, Z. S. Modulation of Charge Density of Nanopore Wall by Salt Gradient and Voltage. *ACS Nano* **2019**, *13*, 9868−9879.
(51) Tsutsui, M.; Yokota, K.; Hsu, W.-L.; Garoli, D.; Daiguji, H.; Kawai, T. Peltier Cooling for Thermal Management in Nanofluidic Devices. *Device* **2024**, *2*, No. 100188.
(52) Yusko, E. C.; An, R.; Mayer, M. Electroosmotic Flow Can Generate Ion Current Rectification in Nano- and Micropores. *ACS Nano* **2010**, *4*, 477−487.
(53) Fu, K.; Han, D.; Kwon, S. R.; Bohn, P. W. Asymmetric Nafion-Coated Nanopore Electrode Arrays as Redox-Cycling-Based Electrochemical Diodes. *ACS Nano* **2018**, *18*, 9177−9185.
(54) Kwon, S.-R.; Fu, K.; Han, D.; Bohn, P. W. Redox Cycling in Individually Encapsulated Attoliter-volume nanopores. *ACS Nano* **2018**, *12*, 12923−12931.

https://doi.org/10.1021/acsnano.5c13339
ACS Nano 2025, 19, 41076−41085